第35卷 第3期 焊 接 学 报 Vol. 35 No. 3
2014年3月 TRANSACTIONS OF THE CHINA WELDING INSTITUTION March 2014

Cu-25Sn-10Ti 活性钎焊 SiO_{2f}/SiO_2 复合材料与 Invar 合金

张大磊[1]， 亓钧雷[1]， 张丽霞[1]， 冯吉才[2]， 梁迎春[3]
(1. 哈尔滨工业大学 先进焊接与连接生产技术国家重点实验室，哈尔滨 150001；
2. 哈尔滨工业大学 山东省特种焊接技术重点实验室，威海 264209；
3. 哈尔滨工业大学 机电工程学院，哈尔滨 150001)

摘 要： 采用 Cu-25Sn-10Ti 钎料钎焊 SiO_{2f}/SiO_2 复合材料与 Invar 合金，研究了界面组织结构及其形成机理，分析了不同钎焊保温时间下界面组织对接头性能的影响. 结果表明，在钎焊温度 880 ℃，保温时间 15 min 的工艺参数下，接头在 SiO_{2f}/SiO_2 复合材料侧与 Invar 合金侧均形成了连续的界面反应层，界面整体结构为 Invar 合金/Fe_2Ti + Cu(s,s) + (Ni,Fe,Cu)$_2$TiSn/Cu(s,s) + $Cu_{41}Sn_{11}$ + CuTi/TiSi + Ti_2O_3/SiO_{2f}/SiO_2 复合材料. 在钎焊温度一定时，随着保温时间的延长，复合材料侧 TiSi + Ti_2O_3 反应层厚度逐步增加，Fe_2Ti 颗粒逐步呈大块状连续依附其上，接头强度先增大后减小. 当钎焊温度 880 ℃，保温时间 15 min 时，接头室温抗剪强度达到 11.86 MPa.

关键词： SiO_{2f}/SiO_2 复合材料； Invar 合金； 钎焊； 界面组织； 抗剪强度
中图分类号： TG454 **文献标识码：** A **文章编号：** 0253－360X(2014)03－0053－04

0 序 言

石英纤维增强二氧化硅陶瓷基复合材料(quartz fiber reinforced SiO_2 composite，SiO_{2f}/SiO_2) 是以二氧化硅陶瓷为基体，二维编织石英纤维为增强相的一种先进航空航天用复合材料. 这种材料具有较高韧性[1]，优良的抗热冲击、承载、透波等性能，且介电损耗小，化学稳定性高，因此在航空航天领域有重大的应用前景[2]. 在实际的应用中，SiO_{2f}/SiO_2 复合材料需要通过一定的连接工艺将其与基体金属相连，因此其连接工艺成为制约该复合材料有效使用的瓶颈. 常用的连接方法包括胶接、机械连接和钎焊[3]. 由于 SiO_{2f}/SiO_2 复合材料加工制备困难，使得机械连接方法难以适用，而胶接接头难以承受飞行体飞行过程中的气动加热. 钎焊接头具有强度高、耐热性能好等优点，因此适合用于连接 SiO_{2f}/SiO_2 复合材料和金属[3-5].

文中自制的 Cu-25Sn-10Ti 是一种含 Ti 元素的活性钎料，用其真空钎焊 SiO_{2f}/SiO_2 复合材料与 Invar 合金研究了钎焊接头的界面微观组织及形成机制，并分析了不同钎焊保温时间下界面组织对接头性能的影响.

1 试验方法

试验用 SiO_{2f}/SiO_2 复合材料为 2.5D 编织结构，具有各向异性，平行纤维编织方向抗剪强度仅 11 MPa，垂直纤维编织方向抗剪强度为 160 MPa. 复合材料与 Invar 合金的表面状态如图 1 所示.

采用金刚石内圆切割机将 SiO_{2f}/SiO_2 复合材料加工成 5 mm×5 mm×5 mm 大小的试样，通过电火花线切割机将 Invar 合金加工成 20 mm×10 mm×3 mm 大小的试样. 采用 200 号、600 号、800 号、1 000 号砂纸逐级打磨试样表面，并在丙酮溶液中超声清洗 20 min 后风化干燥. 自制的 Cu-25Sn-10Ti 活性钎料是将一定比例的铜粉(200 目)、锡粉(300 目)及钛粉(200 目)置于研钵中研磨，混合均匀后采用机械压片机制成规格为 100 mg 的箔片. 通过 DTA 分析得出该钎料的熔点为 780 ℃. 钎焊试样按照 SiO_{2f}/SiO_2 复合材料/Cu-25Sn-10Ti/Invar 合金的顺序进行装配，并采用一定的压力来保证良好的接触. 装配好的试样放置于 Centorr6-1650 型真空炉中进行真空钎焊试验. 通过优化试验确定钎焊温度为 880

收稿日期：2013－03－20
基金项目：国家自然科学基金面上资助项目(51105108，51021002)；中央高校基本科研业务费专项资金资助项目(HIT.NSRIF. 2010113，2010115)；哈尔滨市科技创新人才研究专项基金资助项目(2010RFLXG005)

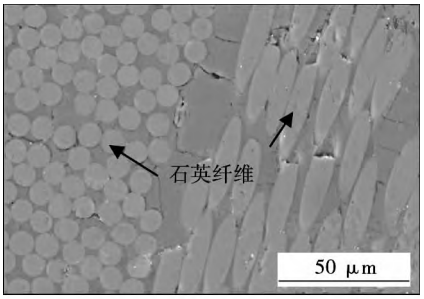

(a) SiO_2f/SiO_2复合材料

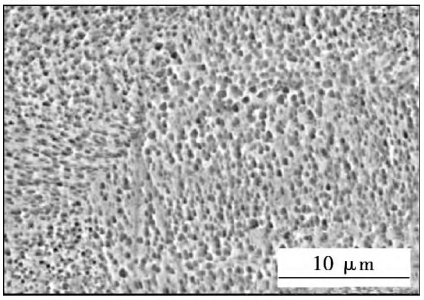

(b) Invar合金

图 1 微观组织形貌

Fig. 1 Microstructure of SiO_{2f}/SiO_2 composite and Invar alloy

℃，按 10 ℃/min 的加热速度加热至该温度，保温一定时间后按 5 ℃/min 的速度降至室温；保温时间分别为 5，15 和 30 min. 钎焊后，采用 Quanta 200FEG 扫描电子显微镜分析钎焊接头界面组织，用其附带的能谱仪（EDS）分析界面各物相成分. 采用旋转阳极 X 射线衍射仪（XRD）对界面产物进行确定. 采用 Instron-5569 电子万能试验机测试钎焊接头抗剪强度.

2 结果与讨论

2.1 接头界面组成及机理分析

图 2 所示为钎焊温度 880 ℃，保温时间 15 min 时接头界面的背散射电子像. 可以看出，钎焊界面完整，无空洞、裂纹等缺陷生成. 在钎焊过程中，钎料与两侧母材均发生反应，界面中形成了多种相，分布于接头各个区域，根据各区域的组织特点，分成 4 个典型区域，即 Invar 合金侧深灰色链条状界面反应区 1、钎缝中近合金侧固溶体区 2、钎缝中近复合材料侧不规则颗粒弥散分布区 3 以及复合材料侧窄条状界面反应区 4.

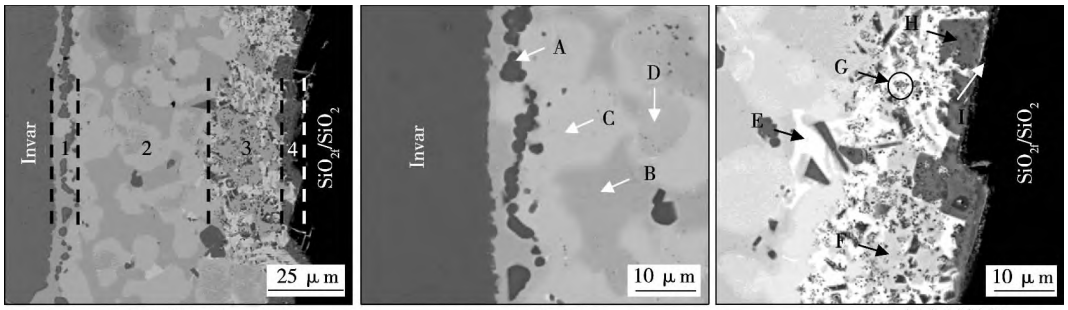

(a) 整体面貌 (b) Invar合金侧 (c) SiO_{2f}/SiO_2复合材料侧

图 2 880 ℃/15 min 时接头界面背散射像

Fig. 2 SEM BEIs of joint brazed at 880 ℃/15 min

图 2b 和图 2c 给出了界面两侧局部放大背散射像，各标注点能谱分析结果如表 1 所示. 在图 2 所示的局部界面中，呈零散分布和链状分布的深灰色块状相（图 2b 中 A，图 2c 中 H）主要由 Fe，Ti 元素构成，且 Fe，Ti 元素原子分数比约为 2∶1，另据文献 [5] 报道，推断该深灰色相为 Fe_2Ti. 区域 2 及区域 3 中的灰色相（图 2b 中 B，图 2c 中 F）中含有大量的 Cu 元素，由相图可以推断该相为 Cu（s，s）. 浅灰色相 C 和 D 中，Fe，Ti，Sn 元素含量大致相等，只是 Ni，Cu 元素的含量略有不同，颜色略有差异，推断其为 $(Ni, Fe, Cu)_2TiSn$. 区域 3 中白色相 E 主要由 Cu，Sn 元素构成，且原子分数比接近 4∶1，参考文献 [7]，推断该相为 $Cu_{41}Sn_{11}$. 焊缝区域 3 中弥散分布的深灰色（较 Fe_2Ti 略浅）颗粒 G 主要构成元素为 Cu，Ti，两者原子比约为 1∶1，同样通过文献 [7]，推断该相为金属间化合物 CuTi. 复合材料侧界面反应层上的 I 相主要包含 Ti，Si，O 三种元素，根据相关文献报道，钎料中 Ti 元素可以与 SiO_2 发生反应，生成（Ti，Si）和 Ti_xO_y 等化合物相；且 I 相中 Si，O，Ti 元素的含量较高，推断其为 TiSi 与 Ti_2O_3. 为了进一步确定界面中各物相，制备了钎缝的 XRD 试样，XRD 测试结果如图 3 所示. 从 XRD 结果中可部分证实上述推断.

综上分析，在钎焊温度 880 ℃，保温 15 min 条件下 SiO_{2f}/SiO_2 复合材料与 Invar 合金的连接接头共有 Cu（s，s），Fe_2Ti，$(Ni, Fe, Cu)_2TiSn$，$Cu_{41}Sn_{11}$，

表 1　图 2 中各区域 EDS 成分分析（原子分数，%）

Table 1　EDS analysis of compositions in Fig. 2

	Fe	Ni	Ti	Sn	Cu	O	Si	可能相
A	59.63	7.33	26.99	2.64	3.41	—	—	Fe_2Ti
B	0.82	—	—	8.97	90.2	—	—	Cu(s,s)
C	13.15	31.03	25.09	23.05	7.62	—	—	$(Ni,Fe,Cu)_2TiSn$
D	14.80	17.36	26.36	20.36	21.12	—	—	$(Ni,Fe,Cu)_2TiSn$
E	4.44	2.08	2.40	18.39	71.72	—	1.58	$Cu_{41}Sn_{11}$
F	2.21	1.01	6.35	8.11	81.53	—	0.79	Cu(s,s)
G	15.74	3.06	28.11	6.55	33.39	—	13.16	CuTi
H	53.38	6.60	35.83	1.39	2.80	—	—	Fe_2Ti
I	1.95	0.54	19.67	1.10	5.54	39.56	31.63	$TiSi+Ti_2O_3$

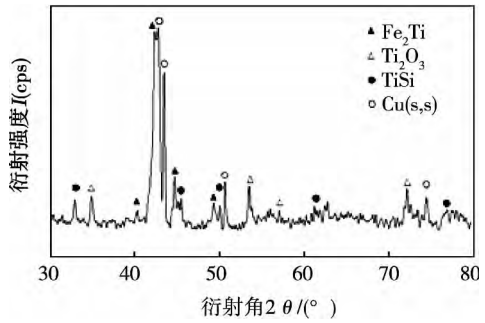

图 3　880 ℃/15 min 时接头的 XRD 分析结果

Fig. 3　XRD pattern of joint brazed at 880 ℃/15 min

CuTi，TiSi 及 Ti_2O_3 几种产物生成. 接头的界面结构可以表示为 Invar/Fe_2Ti + Cu(s,s) + $(Ni,Fe,Cu)_2TiSn$/Cu(s,s) + $Cu_{41}Sn_{11}$ + CuTi/TiSi + Ti_2O_3/SiO_{2f}/SiO_2 复合材料.

根据以上结果，得出高温钎焊阶段接头的形成机理：在钎料熔化后，活性元素 Ti 在液态钎料中的扩散作用增强，一方面，Ti 原子与由 Invar 合金扩散来的 Fe 原子发生反应，生成深灰色斑点状 Fe_2Ti 化合物，随着 Fe_2Ti 量的增多，斑点相互间紧密分布，呈现链状形态；另一方面，与 SiO_{2f}/SiO_2 复合材料表面接触的 Ti 原子与石英纤维反应，生成复合材料侧较薄的 $TiSi+Ti_2O_3$ 反应层；接头中部的 Ti 原子与 Cu 原子发生反应，形成 CuTi 颗粒状化合物. 界面反应的发生可以降低体系能量，根据热力学第二定律，可以通过吉布斯自由能来比较各个反应的驱动力. 根据文献 [8] 及相关数据，得到下列反应的吉布斯自由能（$T=1\ 143$ K），即

$$7Ti+3SiO_2\rightarrow 3TiSi+2Ti_2O_3$$

$$\Delta G_1=-339.314+1.082T\times10^{-3}=-340.550(\text{kJ/mol}) \quad (1)$$

$$Ti+2Fe\rightarrow Fe_2Ti$$

$$\Delta G_2=-103.090+29.011T\times10^{-3}=-69.926(\text{kJ/mol}) \quad (2)$$

$$Ti+Cu\rightarrow CuTi$$

$$\Delta G_3=-17.069+4.887T\times10^{-3}=-11.483(\text{kJ/mol}) \quad (3)$$

由此可见，$\Delta G_1<\Delta G_2<\Delta G_3$，因此反应式(1)，反应式(2)相对反应式(3)进行得更剧烈，程度更大，反应掉大量的 Ti 元素. 这些化合物相随温度降低逐渐凝固，形成以上界面结构.

2.2　保温时间对接头界面组织的影响

保温时间是钎焊的重要工艺参数，它的变化往往引起界面组织结构的变化. 图 4a 和图 4b 分别为钎焊保温 5，25 min 后界面的背散射电子像. 可以看出，两界面组织结构都与保温 15 min 时类似，但随

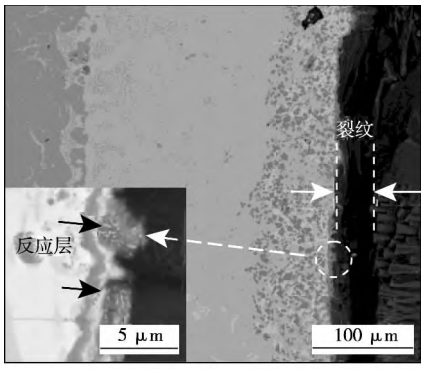

(a) 保温时间5 min

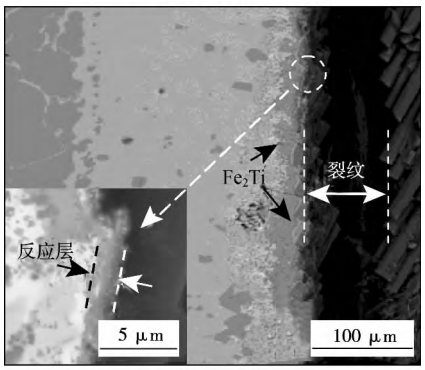

(b) 保温时间25 min

图 4　钎焊保温时间不同时接头背散射像

Fig. 4　SEM BEIs of joints brazed at different holding time

着保温时间的延长，复合材料侧 $TiSi + Ti_2O_3$ 反应层的厚度及 Fe_2Ti 颗粒在该侧的分布状态都发生明显变化. 在保温 5 min 时，$TiSi + Ti_2O_3$ 反应层几乎观察不到，Fe_2Ti 呈小块状零散分布；随着保温时间的延长，$TiSi + Ti_2O_3$ 反应层厚度逐渐增加，Fe_2Ti 颗粒逐渐“长大”；在保温 25 min 时，$TiSi + Ti_2O_3$ 反应层厚度可达 2.5 μm，Fe_2Ti 也逐步依附反应层呈大块状连续分布.

2.3 保温时间对接头抗剪强度的影响

表 2 为保温 5，15 和 25 min 后得到的接头抗剪强度. 可见随着保温时间的延长，接头抗剪强度先增大后降低. 在保温 15 min 时，接头平均抗剪强度达到最高，为 11.86 MPa，断口分析表明断裂主要发生于 SiO_{2f}/SiO_2 复合材料上(图 5). 当保温时间较短时，界面反应不充分，$TiSi + Ti_2O_3$ 反应层过薄，接头中有裂纹存在(图 4a)，难以实现较高的界面结合强度；随着保温时间的延长，界面反应充分，且界面反应层达到一定厚度保证了连接的可靠性；当保温时间进一步延长时，大量的 Fe_2Ti 块状颗粒连续依附在复合材料侧 $TiSi + Ti_2O_3$ 反应层上，导致该反应层两侧区域(即 Fe_2Ti 与 SiO_2) 线膨胀系数相差过大，在降温过程中引起接头开裂(图 4b)，抗剪强度降低.

表 2 不同保温时间接头抗剪强度

Table 2 Shear strength of joints at different holding time

保温时间 t/min	抗剪强度 R_τ/MPa			平均抗剪强度 $\overline{R}_\tau$/MPa
5	8.85	7.94	8.14	8.31
15	10.92	12.35	12.31	11.86
25	6.89	5.97	5.83	6.23

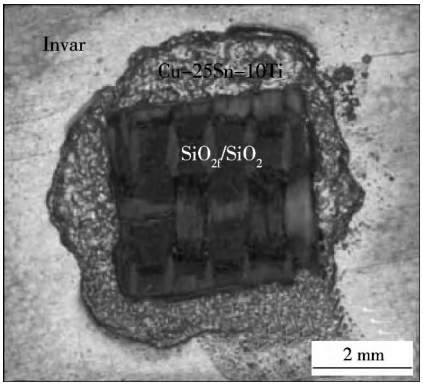

图 5 880 ℃/15 min 时接头断口

Fig. 5 Structure of joint brazed at 880 ℃/15 min

3 结 论

(1) 采用自制的 Cu-25Sn-10Ti 钎料钎焊 Invar 合金与 SiO_{2f}/SiO_2 复合材料，在钎焊温度 880 ℃，保温 15 min 时，接头的界面结构为 Invar 合金/Fe_2Ti + Cu(s,s) + (Ni,Fe,Cu)$_2$TiSn/Cu(s,s) + $Cu_{41}Sn_{11}$ + CuTi/TiSi + Ti_2O_3/SiO_{2f}/SiO_2 复合材料.

(2) 在保温 5 min 时，复合材料侧 $TiSi + Ti_2O_3$ 反应层过薄，且存在裂纹，接头强度较低；随着钎焊保温时间的延长，复合材料侧 $TiSi + Ti_2O_3$ 反应层厚度逐渐增加且连续，在保温 15 min 时，该层厚度合适，接头平均抗剪强度达到 11.86 MPa；在保温 25 min 时，该层厚度达到 2.5 μm，Fe_2Ti 颗粒逐步呈大块状连续依附于该反应层上，由于该层两侧相邻区域线膨胀系数相差过大，在降温过程中引起接头开裂，接头强度降低.

参考文献:

[1] 刘 多，张丽霞，何 鹏，等. SiO_2 玻璃陶瓷与 TC4 钛合金的活性钎焊[J]. 焊接学报，2009，30(2)：14－16.
Liu Duo，Zhang Lixia，He Peng，*et al*. Active brazing of SiO_2 glass ceramic to TC4 alloy [J]. Transactions of the China Welding Institution，2004，30(2)：14－16.

[2] Schmidt S，Beyer S，Knabe H，*et al*. Advanced ceramic matrix composite materials for current and future propulsion technology applications [J]. Acta Astronautica，2004，55(5)：409－420.

[3] Zhao Lei，Zhang Lixia，Tian Xiaoyu，*et al*. Interfacial microstructure and mechanical properties of joining electroless nickel plated quartz fibers reinforced silica composite to Invar [J]. Materials and Design，2011，32：382－387.

[4] 赵 磊，张丽霞，田晓羽，等. 化学镀表面改性石英纤维复合材料与因瓦合金的真空钎焊[J]. 焊接学报，2010，31(4)：9－12.
Zhao Lei，Zhang Lixia，Tian Xiaoyu，*et al*. Vacuum brazing of nickle-plated quartz fiber reinforced SiO_2 composites and Invar [J]. Transactions of the China Welding Institution，2010，31(4)：9－12.

[5] 赵 磊，张丽霞，田晓羽，等. 石英纤维复合材料与因瓦合金的活性胶辅助钎焊连接[J]. 焊接学报，2010，31(6)：49－52.
Zhao Lei，Zhang Lixia，Tian Xiaoyu，*et al*. Active cement added brazing of quartz fibers reinforced silica composites to Invar alloy [J]. Transactions of the China Welding Institution，2010，31(6)：49－52.

[6] Kliauga A M，Travessa D，Ferrante M. Al_2O_3/Ti interlayer/AISI304 diffusion bonded joint：microstructural characterization of the two interfaces [J]. Materials Characterization，2001，46(1)：65－74.

[7] Yuchan H，Shuntian L. Microstructural development of Cu-Sn-Ti alloys on graphite [J]. Journal of Alloys and Compounds，2008，466：126－132.

[8] 李 真. 炼钢常用图表数据手册[M]. 北京：冶金工业出版社，1998.

作者简介： 张大磊，男，1988 年出生，硕士研究生. 主要从事钎焊、新材料连接研究工作. 发表论文 3 篇. Email：hitzhangdl@126.com

通讯作者： 张丽霞，女，副教授. Email：zhanglxia@hit.edu.cn

Abstract: A coupled thermal-mechanical FE (finite element) model of 7A52 aluminum alloy TANDEM welding and a simplified FE model for single-GCr15 shot impact simulation were developed separately. The element size of welded joint region which was impacted by shots was amplified reasonably. Based on the premise, the numerical results would not be affected by this simplification. The computational results of welding residual stress were obtained, and the influences of ball's dimension and impact velocity on induced residual stresses were analyzed subsequently. On the basis, the coupling computation of residual stress field in aluminum alloy welded joint and the shot peening treatment were performed by means of data transfer based on the standard and explicit solver of ABAQUS software. The computational results showed that the residual stresses on the surface and depth direction of welded joint were improved remarkably after shot peening.

Key words: aluminum alloy; welded joint; shot peening; finite element method; residual stress

Study on vacuum brazing of DD3 Ni-base superalloy and Ti_3AlC_2 ceramic LIU Jiakun[1], QI Junlei[1], CAO Jian[1], LIN Xingtao[2], WANG Zhijie[1], FENG Jicai[3] (1. State Key Laboratory of Advanced Welding and Joining, Harbin Institute of Technology, Harbin 150001, China; 2. Zhejiang Provincial Special Equipment Inspection and Research Institure, Hangzhou 310020, China; 3. Shandong Provincial Key Laboratory of Special Welding Technology, Harbin Institute of Technology at Weihai, Weihai 264209, China). pp 41 - 44

Abstract: By comparison, an appropriate brazing filler metal was selected and applied to the follow-on experiments. DD3 Ni-base superalloy and Ti_3AlC_2 ceramic were successfully brazed in vacuum using Ag-Cu-Ti as filler metal in a temperature range of 800 ~ 900 ℃ for 10 min. The interfacial microstructure of the brazed joints was investigated by adopting scanning electron microscope, energy dispersive spectroscopy and X-ray diffraction. The result showed that the typical interfacial microstructure of the joints can be described as DD3/AlNi/Al_3(Ni, Cu)$_5$ + Al(Ni, Cu) + Ag_{ss}/(Al, Ti)$_3$(Ni, Cu)$_5$/Al_4Cu_9 + $AlNi_2Ti$ + Ag_{ss}/TiAg/Ti_3AlC_2. Through the mechanical properties test of the joints, a maximum shear strength value of 135.9 MPa was obtained when the joint was brazed at 850 ℃ for 10 min. The fracture occurred at the Ti_3AlC_2 ceramic side adjacent to the brazed seam during the shear test. The interfacial microstructure of the joints was similar to each other, while the shear strength decreased when reduces or improves the brazing temperature.

Key words: superalloy; ceramic; brazing; interfacial microstructure; shear strength

Experimental and simulation analysis on shear fracture for BGA solder ball under different strain rates XUE Mingyang, WEI Guoqiang, JIN Liang, WANG Haiyan (School of Mechanical and Automotive Engineering, South China University of Technology, Guangzhou 510640, China). pp 45 - 48

Abstract: Influence of thermal aging time on the morphology and microstructure of the interfacial IMC for BGA (ball grid array) package between Sn-3.0Ag-0.5Cu lead-free solder ball and Cu interface at 115 ℃ were investigated. Meanwhile, the shear strength for BGA solder ball was studied and simulated by ANSYS 12.0 finite element software with a non-linear finite element model under two different strain rates. The experimental results are as follows: with the increase of the aging time, the morphology of interfacial IMC changes from dendritic to continuous even lamellar, the thickness of interfacial IMC increases continuously and the shear strength of solder ball gradually decreases. Furthermore, the simulation results show that the larger strain rate will result in the higher shear strength, the higher Von Mises stress, the smaller plastic strain and the higher plastic strain energy density.

Key words: BGA package; shear strength; strain rate; finite element analysis

Acoustic field modeling of ultrasonic-arc hybrid welding system and analysis of ultrasonic-aided arc pressure WANG Bin[1], SUN Qingjie[1,2], CHENG Wenqian[1], FENG Jicai[1] (1. Shandong Provincial Laboratory of Special Welding Technology, Harbin Institute of Technology at Weihai, Weihai 264209, China; 2. State Key Laboratory of Advanced Welding and Joining, Harbin Institute of Technology, Harbin 150001, China). pp 49 - 52

Abstract: Acoustic field analysis of space wave propagation used for ultrasonic-aided TIG welding was proposed and finite element simulation analysis of sound field variation with acoustic emission radius and that of the acoustics parameters variation with arc length was employed with COMSOL. Besides, a new model was also established for ultrasound-aided TIG welding characteristics. Distribution of arc pressure for stable combustion DC U-TIG arc and that of conventional TIG arc under different welding parameters were measured experimentally by using a hole drilling method. The result reveals that arc peak pressure of DC U-TIG is significantly higher than that of conventional TIG, which illustrates that the effect of hybrid-arc can enhance the arc pressure above the surface of weld pool, but the D-value between them decreases with the welding current increases. Preliminary analysis suggests that when high welding current is employed, the high temperature and large current density in the central area of arc column greatly improve the arc peak pressure of conventional TIG. In contrast, the increase of arc peak pressure is reduced with the increase of weld current because plasma flow force of welding arc is limited by gas-flow rates.

Key words: ultrasonic hybrid; acoustic field modeling; arc pressure

Active brazing of SiO_{2f}/SiO_2 composite and Invar alloy with Cu-25Sn-10Ti ZHANG Dalei[1], QI Junlei[1], ZHANG Lixia[1], FENG Jicai[2], LIANG Yingchun[3] (1. State Key Laboratory of Advanced Welding and Joining, Harbin Institute of Technology, Harbin 150001, China; 2. Shandong Provincial Key Laboratory of Special Welding Technology, Harbin Institute of Technology at Weihai, Weihai 264209, China; 3. School of Mechatronics Engineering, Harbin Institute of Technology, Harbin 150001, China). pp 53 - 56

Abstract: The Invar alloy was brazed to SiO_{2f}/SiO_2 com-

posite using Cu-25Sn-10Ti filler alloy. The interfacial microstructure of joint was analyzed and its formation mechanism was discussed, and also the impact of interfacial microstructure on shear strength of joints at different holding time was studied. Results show that continuous interfacial reaction layer has been formed at both sides of the base materials at brazing temperature 880 ℃ and holding time for 15 min, while the typical interfacial microstructure was Invar alloy/Fe_2Ti + Cu(s,s) + (Ni, Fe, Cu)$_2$TiSn/Cu(s,s) + $Cu_{41}Sn_{11}$ + CuTi/TiSi + Ti_2O_3/SiO_{2f}/SiO_2 composite. Holding time increasing would enlarge the thickness of TiSi Ti_2O_3 layer near SiO_{2f}/SiO_2 composite, and Fe_2Ti particles would turn into blocks. The shear strength of joint would also change with increasing of holding time. The shear strength of the joints reaches a maximum of 11.86 MPa when the temperature is 880 ℃ and the holding time is 15 min.

Key words: SiO_{2f}/SiO_2 composite; Invar alloy; brazing; interfacial microstructure; shear strength

In-situ observation of cracking in wollastonite coatings and effect of powder size on fracture WANG Lubin, WANG Weize, CHEN Yufan, XUAN Fuzhen (Key Laboratory of Pressure Systems and Safety, Ministry of Education, East China University of Science and Technology, Shanghai 200237, China). pp 57 – 60

Abstract: Fracture analysis of coatings has an important role on the investigation of coating's failure mechanism, the optimization of the processing parameters and the design. The fracture of plasma sprayed wollastonite coatings was observed in-situ by using a scanning electron microscope (SEM) during the tapered double cantilever beam (TDCB) specimens were pulled open. Additionally, the effect of powder size on the coating's fracture toughness is investigated based on the observation of the microstructure, fracture morphology and cracking propagation of coatings. It was found that the cracking path was mainly influenced by the applied stress. The original pores in the coatings, including the large pores, cracks and non-bounded interfaces could guide the cracking somewhat. The fracture toughness of coatings increased and fracture paths were more curved with the decreasing of powder size

Key words: coating fracture; in-situ observation; wollastonite; plasma spraying

Linear cumulative damage analysis of welded joints under combined cycle fatigue ZHANG Tao, WANG Dongpo, DENG Caiyan, WU Liangchen (School of Material Science and Engineering, Tianjin University, Tianjin 300072, China). pp 61 – 65

Abstract: 16Mn steel welded joints are tested to fail under low cycle fatigue, high cycle fatigue and combined cycle fatigue using an apparatus that is capable of providing interactive loading. A linear cumulative damage theory is used to estimate the fatigue life of the butt joints. The proportion of each of the two fatigue load components which cause the cumulative damage is calculated. The research indicate that high cycle fatigue loads and low cycle fatigue loads simply calculated as proportion would seriously underestimate the coupling between the two components of the fatigue load when we use Miner rule to calculate the fatigue cumulative damage of specimens. However, we can take into account of the coupling between the high and low cycle fatigue loads when we turn to the outsourcing envelope of the low cycle fatigue loads.

Key words: welded joints; combined cycle fatigue; linear cumulative damage

Characteristic of temperature distributions in stirring tools during friction stir welding LI Jingyong, ZHAO Yangyang, KANG Xiaoliang (Advanced Welding Technology Provincial Key Laboratory, Jiangsu University of Science and Technology, Zhenjiang 212003, China). pp 66 – 70

Abstract: The temperature distribution in stirring tools was measured by experimental method. It is shown that the characteristic of temperature distribution in stirring tools is much different from that in workpieces. At the beginning stage of friction stir welding, the softening in stirring zone reduces the friction coefficient and the friction heat between the stirring pin and the workpiece, so the temperature in stirring tools stops rising, whereas decreases in the exterior margin of the tool before the shoulder touches the workpiece. At the steady welding stage, equilibrium exists between the heat quantity delivered to and dissipated through the stirring tool, and its temperature keeps little fluctuation. The surface of the high-speed rotating tool has intensive heat exchange with the air around it, so the temperature near its axis is higher than that on the exterior margin. The stirring tools made of metal with lower specific heat capacity and higher coefficient of heat transfer lead to heat within the welding area dissipating faster.

Key words: friction stir welding; stirring tool; temperature field

A novel composite control strategy for plasma cutting power supply based on arc control SUN Qiang, CHEN Long, CHEN Guitao, WANG Huamin (Automation & Information Engineering College, Xi'an University of Technology, Xi'an 710048, China). pp 71 – 75

Abstract: This paper analyzes static characteristics of plasma arc with the derivation of plasma arc mathematical model according to the application of low-frequency (LF) pilot arc technology in the plasma cutting power supply, and integrates with the control requirements in low-frequency (LF) pilot arc, arc transferring and arc energy transferring, and proposes a novel composite control strategy. In order to meet the power's control requirements of rapidity and stability with the load of low-frequency (LF) pilot arc, the inner loop of this strategy builds up voltage loop composite control with feed-forward arc voltage and feedback arc voltage, and the current outer loop controls the energy of plasma arc, forming a control method of feed-forward composite control of double closed-loop. Simulations and experiments were given to verify that the mentioned control strategy not only improved system's stability and robustness, but also had excellent dynamic responsibility. The power had well non-liner resilience, meeting requirements for plasma cutting power supply.

Key words: plasma cutting power supply; arc control;